Seismic Performance of Piled Raft Foundation with Grid-Form DMWs under Large Earthquake Load

格子状地盤改良を併用したパイルド・ラフト基礎の大地震時における耐震性について

Yoshimasa Shigeno 重野 喜政*1 Kiyoshi Yamashita 山下 清*2 Junji Hamada 濱田 純次*3

Summary

Nonlinear seismic response analyses are conducted to evaluate seismic performance of a piled raft foundation with grid-form deep mixing walls (DMWs) under a large earthquake load. The 12-story base-isolated building is modeled using a detailed three dimensional building-soil interaction model by finite element method. The ground is modeled using a multi-surface elasto-plastic model, and the DMWs are modeled using the nonlinear elastic model that has tensile and shear criteria. First, the numerical model is fitted to the observation records of the 2011 off the Pacific coast of Tohoku Earthquake. Then, the analysis is conducted using a large earthquake that is notified as Level 2 earthquake by the Japanese building design code. As a result of the analysis, it is found that the grid-form DMWs are quite effective in reducing the sectional force of piles to an acceptable level, even if the induced stress in the DMWs partially fails during the large-scale earthquake.

Keywords: piled raft foundation, grid-form DMWs, large earthquake, soil and structure interaction analysis, performance-based design

梗　概

格子状地盤改良を併用したパイルド・ラフト基礎の大地震に対する耐震性能を解析的に検討した。軟弱地盤上の12階建て免震建物を対象とし，詳細な3次元建物・地盤連成系有限要素によりモデル化した。地盤には，ひずみ依存特性に基づく弾塑性モデルを用い，改良土には，引張強度とせん断強度の2つの破壊規準を持つ非線形モデルを用いた。初めに，東日本大震災時における観測データを用いて解析モデルとのマッチングを行い，引き続いて大地震を用いた検討を行った。入力地震波には，レベル2告示波神戸位相を用いた。検討の結果，格子状地盤改良の一部に引張破壊が生じるが，改良体の機能は保持され，杭の断面力は許容値以下になることがわかった。

キーワード：パイルド・ラフト基礎，格子状地盤改良，大地震，相互作用解析，性能設計

1 INTRODUCTION

In recent years, piled raft foundations have been used in many countries as building foundations. The effectiveness of piled rafts at reducing average and differential settlements has been confirmed on soft clay and even on liquefiable sand with grid-form cement deep mixing walls (DMWs) (Yamashita et al., 2011, 2012, 2016). The grid-form DMWs work not only as a countermeasure of liquefaction to increase the resistance of unstabilized soil but also as a resistance component against the horizontal load. However, adding the grid-form DMWs to piled rafts as a new component, the seismic behavior becomes more complicated and the necessity for detailed evaluation increases.

To investigate the seismic response of a piled raft foundation with grid-form DMWs, field monitoring has been performed on the piled raft system in soft ground supporting a 12-story building. The seismic response of the soil-foundation system was successfully recorded at the time of the 2011 off the Pacific coast of Tohoku Earthquake (the 2011 Tohoku earthquake)

＊1 Group Leader, Research & Development Institute 技術研究所 構造部 応用数理グループ長
＊2 Executive Manager, Research & Development Institute, Dr. Eng. 技術研究所 専門役 博士(工学)
＊3 Chief Researcher, Research & Development Institute, Dr. Eng. 技術研究所 地盤・基礎部 主任研究員 博士(工学)

(Yamashita et al., 2012). The seismic response analysis using a detailed three-dimensional finite element model was conducted using equivalent linear moduli by Onimaru (2012) and Hamada (2014), and the analytical results agreed well with the observation records of the 2011 Tohoku earthquake. Simulation analysis for the observation records using nonlinear soil model was also conducted (Shigeno, 2015), and then the analysis under the large earthquake loads was conducted in the previous study (Shigeno et al., 2015). The effectiveness of the DMWs in reducing sectional force of the piles was confirmed even though the partial failure occurred in the DMWs under large earthquake load in the study. However, there was some difference in the sectional forces of the piles between the analysis and the observations, and there was some lack of consistency on the modeling of the stabilized soil in the analyses for the medium and large earthquakes.

In this paper, first, in order to determine more suitable deformation parameters of the stabilized soil as well as the unimproved soil to simulate the observation records more accurately, seismic response analysis of the piled raft system was conducted again. Then, the dynamic analysis under a large earthquake is conducted using the more suitable deformation parameters, and the seismic performance of the piled raft system is discussed focusing on the effect of the grid-form DMWs on the sectional force of the piles.

2 BUILDING AND GROUND CONDITIONS

Figure 1 shows a schematic view of the building and its foundation with the soil profile. The building analyzed is a 12-story residential building located in Tokyo. The soil down to a depth of 44m is alluvial stratum. The soil profile down to the depth of 7 m is made of fill, soft silt and loose silty sand where the ground water table appears approximately 1.8 m below the ground surface. The building is supported by a piled raft with grid-form DMWs which were employed to prevent liquefaction of the silty sand from GL -3 m to -7 m as well as to improve the bearing capacity of the raft foundation. Figure 2 shows the foundation plan. The spacing between the DMWs is about 6 to 9 m, and the area replacement ratio is 25%. The soil conditions, the foundation design and the instrumentation, as well as the seismic response of the soil-foundation-structure system, were reported by Yamashita et al. (2012).

3 NUMERICAL ANALYSIS

3.1 Finite element mesh

Figure 3 shows the finite element (FE) mesh, which is the same as that used in the previous study. The superstructure is modeled using elastic bars and shells, and the piles are modeled using elastic bars. Table 1 shows the dimensions and material properties of the piles. The raft is modeled using elastic solid elements with the modulus of concrete. Rayleigh damping is

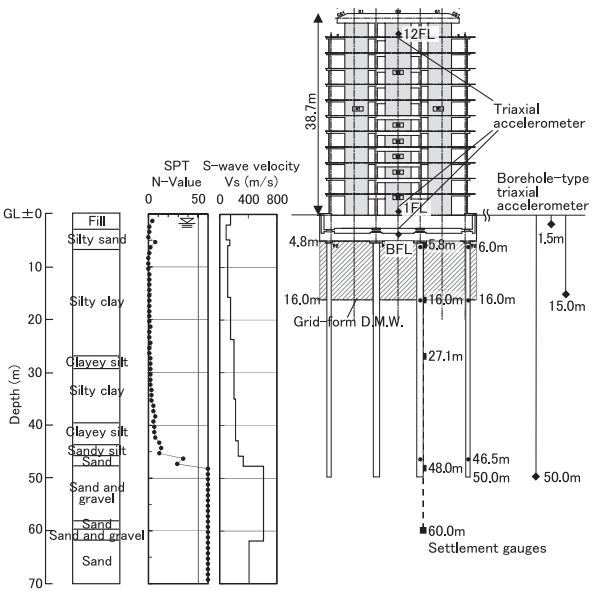

Fig. 1 Schematic of the building and foundation with soil profile

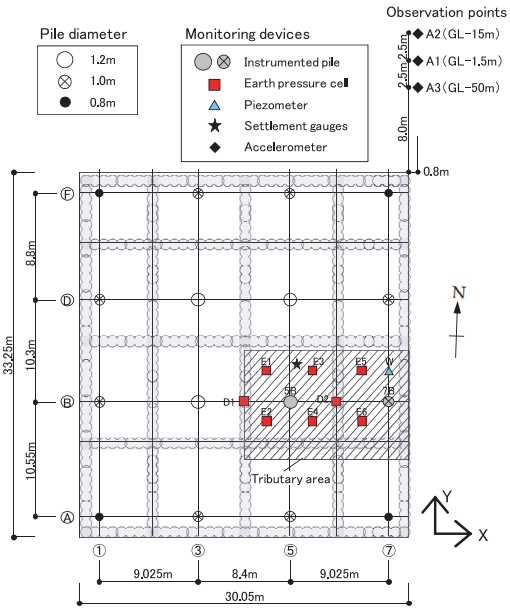

Fig. 2 Foundation plan with locations of monitoring devices

Table 1 Dimensions and material properties of piles

Pile diameter (mm)	Young's modulus (MPa)	Density ρ (t/m^3)	Damping (%)	A_e of SC pile (m^2)	I_e of SC pile (m^4)	A_e of PHC pile (m^2)	I_e of PHC pile (m^4)
800	40000	2.5	2.0	0.3268	0.02199	0.2441	0.01455
1000	40000	2.5	2.0	0.4649	0.04899	0.3633	0.03437
1200	40000	2.5	2.0	0.6714	0.6714	0.5054	0.06958

Ae : Equivalent cross-sectional area
Ie : Equivalent area moment of inertia

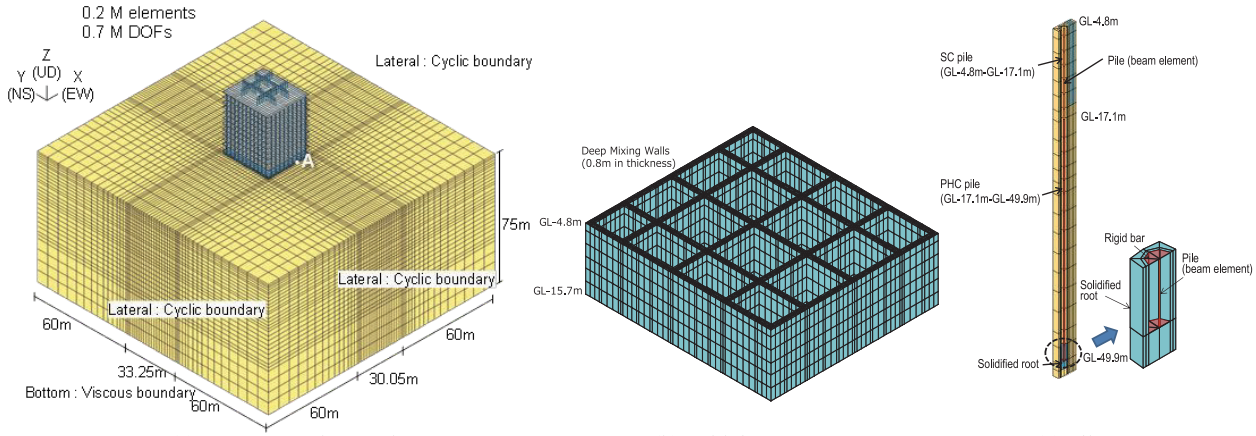

(a) Structure and ground (b) Grid-form DMWs (c) Pile

Fig. 3 FE mesh of soil-foundation-superstructure model

applied to these components at a damping ratio of 2%.

Figure 4 shows a top view of the FE mesh beneath the raft. To consider the shape and volume of the piles, cavities in the shape of the piles are made in the model. The nodes of the piles and the adjacent ground nodes at the same depth are bound by rigid bar elements. The base isolation system is modeled using a tri-linear spring (Hamada et al., 2014). The lateral boundaries are periodic boundaries, and are positioned 60 m outside of the building to minimize the boundary effect. The bottom is a viscous boundary at a depth of 75 m from the ground surface. The software is an in-house program called MuDIAN (Shiomi et al., 1998). It is parallelized using the hybrid parallel method and is able to analyze a large-DOF model at high speed (Shigeno et al., 2014).

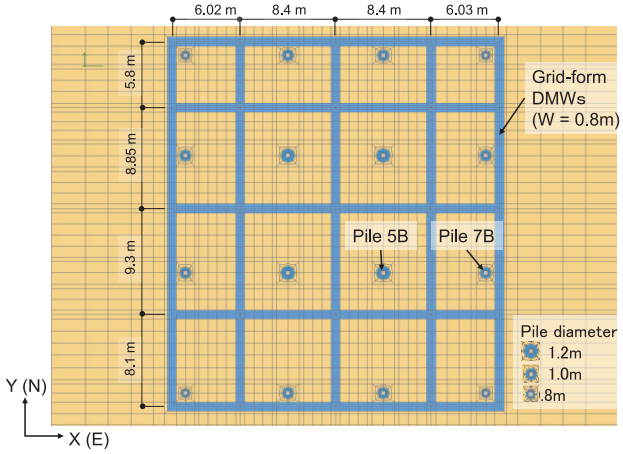

Fig. 4 Top view of FE mesh for piles and grid-form DMWs

3.2 Constitutive model and properties for soil

A multi-hardening model proposed by Shiomi and Fujiwara (2014) is used as the constitutive model for the soil, as in the same way as the previous study. Hardening parameter is calculated using the tangential shear modulus that is evaluated from the *G*-γ characteristics (Shigeno 2015). The shear strength of the Mohr-Coulomb model is given as cohesion. The cohesion of layers except for being investigated is calculated using γ_{50} of the *G*-γ characteristics.

The shear wave velocity profile of the ground is obtained using an optimization method targeted small earthquakes (Onimaru et al., 2012). The optimized V_S distribution is shown in Fig. 5 with the logged V_S. Initial damping other than the damping induced by the constitutive model is assumed 1%, and is given by Rayleigh damping. Table 2 shows the soil properties, and the nonlinear characteristics are shown in the later section. In this analysis, liquefaction is not considered. Further research is necessary to examine the effect of it.

Table 2 Soil properties

Layer upper depth (m)	Layer bottom depth (m)	Stratum	Density (t/m^3)	Initial shear modulus (kPa)	Poisson's ratio
0.0	2.0	Fill	1.70	25,442	0.467
2.0	4.8	Silty clay	1.60	19,948	0.496
4.8	5.9	Silty sand	1.80	28,945	0.490
5.9	7.9	Silty sand	1.60	29,987	0.495
7.9	11.7	Silty clay	1.60	24,522	0.495
11.7	15.7	Silty clay	1.60	27,198	0.496
15.7	19.7	Silty clay	1.60	45,610	0.495
19.7	23.7	Silty clay	1.60	45,959	0.495
23.7	27.1	Silty clay	1.60	62,637	0.491
27.1	32.3	Silty clay	1.60	67,240	0.491
32.3	35.0	Silty clay	1.60	93,912	0.491
35.0	37.6	Silty clay	1.70	159,801	0.490
37.6	40.2	Silty clay	1.70	202,821	0.490
40.2	42.9	Silty clay	1.70	205,883	0.490
42.9	45.8	Clayey silt	1.70	230,470	0.487
45.8	47.7	Sand	1.80	245,197	0.479
47.7	49.9	Sand and grabel	1.80	671,011	0.458
49.9	61.9	Sand and grabel	2.00	745,621	0.458
61.9	75.0	Sand	2.00	749,513	0.471

Table 3 Properties of stabilized soil and parameter of Hayashi－Hibino model

Density ρ (t/m^3)	Tensile strength σ_t (kPa)	Cohesion c (kPa)	Friction angle ϕ (degree)	Shear modulus G_0 (MPa)	ν	Damping h (%)	Parameter a
2.0	760	1140	30	500	0.26	5.0	1.0

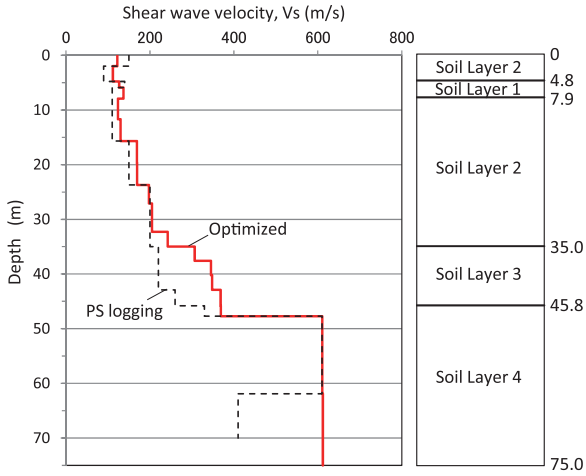

Fig. 5 Profile of optimized initial shear wave velocity from P-S logging

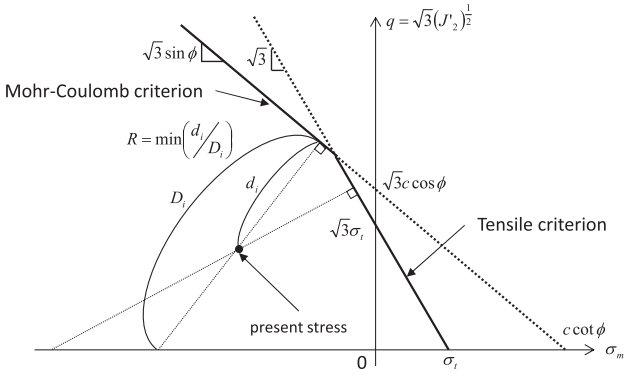

Fig. 6 Criteria of Hayashi-Hibino model

3.3 Constitutive model and properties for stabilized soil

The failure mode of the DMWs during an earthquake is tension or shear. The Mohr－Coulomb model is often applied to stabilized soil, but it generally gives a larger tensile strength than the real value. The tensile criterion has to be used for correct evaluation. The tensile criterion σ_t is expressed by the maximum principal stress σ_1 (note that tension is positive) and it is expressed by stress invariants J'_2 and σ_m by applying a Lode angle θ ($-\pi/6<\theta<\pi/6$)

$$\sigma_t=\sigma_1=\frac{2(J'_2)^{\frac{1}{2}}}{\sqrt{3}}\sin\left(\theta+\frac{2\pi}{3}\right)+\sigma_m \quad (1)$$

where J'_2 is the second invariant of deviatoric stress, and σ_m is the mean stress. Also, the Mohr－Coulomb criterion for the shear failure is expressed using stress invariants as follows

$$\sigma_m \sin\phi + (J'_2)^{\frac{1}{2}}\left(\cos\theta - \frac{1}{\sqrt{3}}\sin\theta\sin\phi\right) = c\cos\phi \tag{2}$$

where ϕ is the friction angle and c is the cohesion. These criteria are shown in Fig. 6. The tensile strength is evaluated correctly by taking a lower strength between the two criteria.

The Hayashi − Hibino model (Motojima et al., 1978) is used for the two-criterion model described here in this study. The Hayashi − Hibino model is a nonlinear elastic model, and the elastic modulus is reduced to the specified value at failure. This model is able to evaluate nonlinearity within the failure criteria. The proximity ratio to the criteria R defined in Fig. 6 is used. R takes the minimum value for the two criteria and becomes 0 when the stress reaches the criteria. The elastic moduli are reduced according to R in the following equations using the parameter a.

$$E = R^{1/a}E_0, \quad 0.45 - \nu = R^{1/2a}(0.45 - \nu_0) \tag{3}$$

The properties of the stabilized soil used in the Hayashi − Hibino model are shown in Table 3. The tensile strength and the cohesion are set to $0.2q_u$ and $0.3q_u$, respectively, where the unconfined compressive strength of the stabilized soil, q_u, was determined based on the results of unconfined compression tests on 36 core samples curing for four weeks, and set at the average value of 3.8 MPa (Yamashita et al., 2015). The friction angle is assumed to be 30 degrees.

The initial shear modulus is adjusted to the observation records in the later section. The initial stress of the DMWs is not considered here.

4 ANALYSIS RESULTS

4.1 Seismic simulation for the 2011 Tohoku earthquake

The nonlinear analysis was conducted using the input motion based on the records of the 2011 Tohoku earthquake. Figure 7 shows the input motion in each direction. The input motions are categorized as a medium earthquake considering the recorded peak ground acceleration of 1.75 m/s^2 near ground surface shown in Fig. 12. In the analysis, two deformation parameters of the soils are examined. One is nonlinearity of the soil and the stabilized soil, and the other is the initial shear modulus of the stabilized soil. The nonlinear characteristics of the unimproved soil were obtained from the cyclic triaxial tests of in-situ samples as shown in Fig. 8.

When the nonlinear characteristics shown in Fig. 8 was first applied following the profile in Fig. 5, it was found that the analytical peak displacement was somewhat larger than the observations, and this also induced the difference of the bending moment at GL -16 m from the observation. This can be attributed to using the same G-γ characteristic from the sample at a depth of 12.2 m for very wide range of soft silty clay layer between depths of 7.9 and 35.0 m (Soil Layer 2 in Fig. 5 and Fig. 8). Hence, the G-γ characteristic from GL -11.7 m to GL -35.0 m was made slightly harder to reproduce the observation records. Finally, the γ_{50} of these layers were doubled, and the modified Hardin − Drnevich model was applied as shown in Fig. 8.

In the previous study, the initial shear modulus G_0 of the stabilized soil was set to 700 MPa based on the design standard

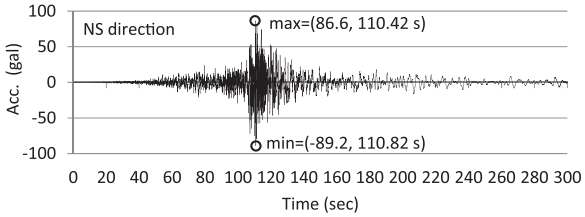

(a) NS direction

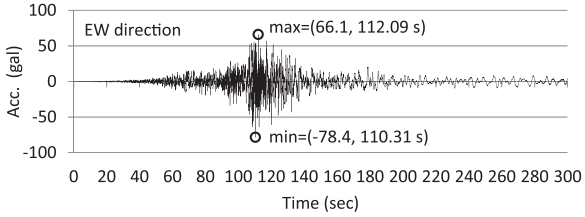

(b) EW direction

Fig. 7 Input motion at a depth of 75 m (2E), based on records of the 2011 earthquake

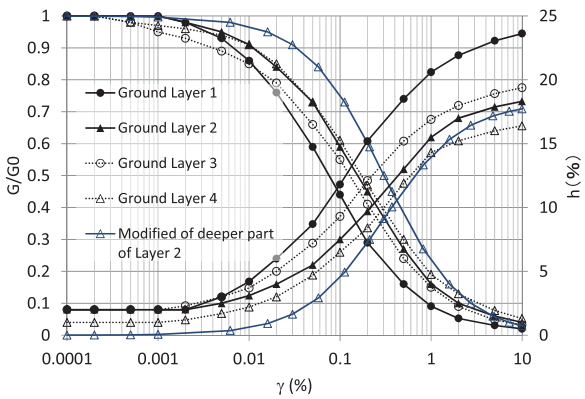

Fig. 8 Strain dependence characteristics of soil

strength of 1.8 MPa referred to the exiting studies. And the same constitutive model for the soil was applied to the stabilized soil, considering that the induced stress did not cause tensile failure. The analytical results fairly agreed well with the observations. However, there were some differences between the observations and the analysis, especially in the maximum bending moments near the pile head. In addition, tensile failure should be considered in the analysis under the large earthquake load.

Therefore, the initial shear modulus G_0 of the stabilized soil is adjusted to fit the maximum bending moments near the pile head in the analysis to those of the observations, and the Hayashi-Hibino model for the stabilized soil is also used in the analysis using the observation records of the 2011 Tohoku earthquake. Nonlinearity of the stabilized soil is referred to the experiments by Kuroda (2001). The G-γ characteristic derived from the experiments was used as a target of the numerical simple shear test. The parameter a of the Hayashi－Hibino model in equation (3) was determined for each initial shear modulus. Figure 9 shows the target nonlinearity and the result of the numerical test when the initial G_0 was 500 MPa (G_0 = 700 MPa in the previous analysis). Damping of the stabilized soil is needed because the applied model is nonlinear elastic. As the damping ratio of the stabilized soil is somewhat high at the small strain compared to unimproved soils (Kuroda et al., 2001), the damping ratio was set to 5%.

The simulation results against the observations are shown in Figs. 10 to 13. Figure 10 shows the time history of the seismic response of the ground surface (at a depth of 1.5 m) at the observation point in the EW direction during the principal motion (100 to 140 s). The acceleration and displacement in the analysis show good agreement with those of the observations. Figure 11 shows the time history of the bending moment of Pile 5B near the pile head and at a depth of 16 m (bottom level of the DMWs). The bending moments in the analysis also agree well with those of the observations, although the bending moment at

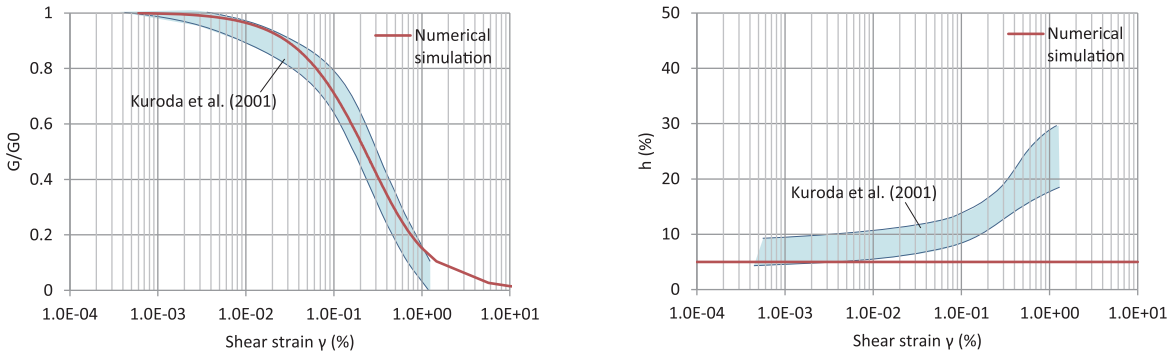

(a) G/G_0 (b) h

Fig. 9 Strain dependence characteristics of stabilized soil

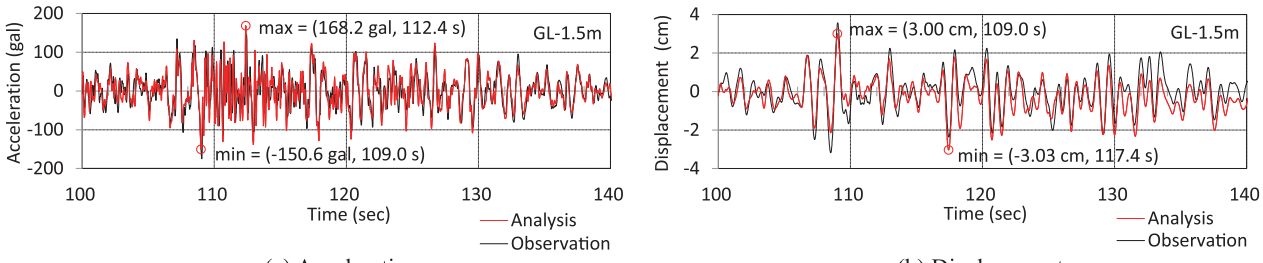

(a) Acceleration (b) Displacement

Fig. 10 Time history of ground surface response

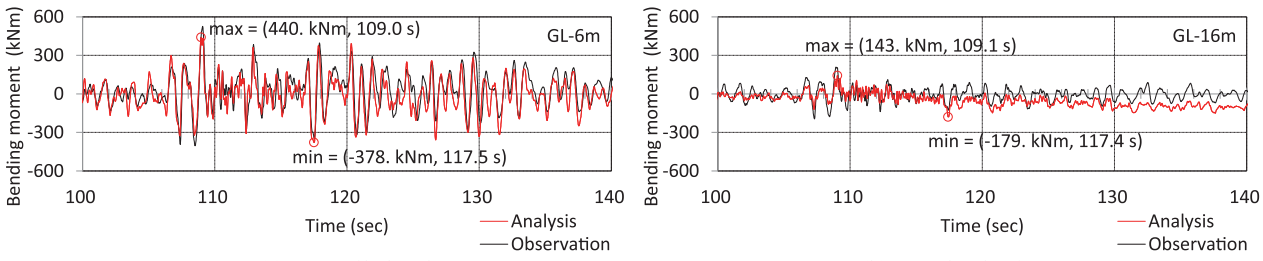

(a) Near pile head (b) At a depth of 16m

Fig. 11 Time history of bending moment of Pile 5B

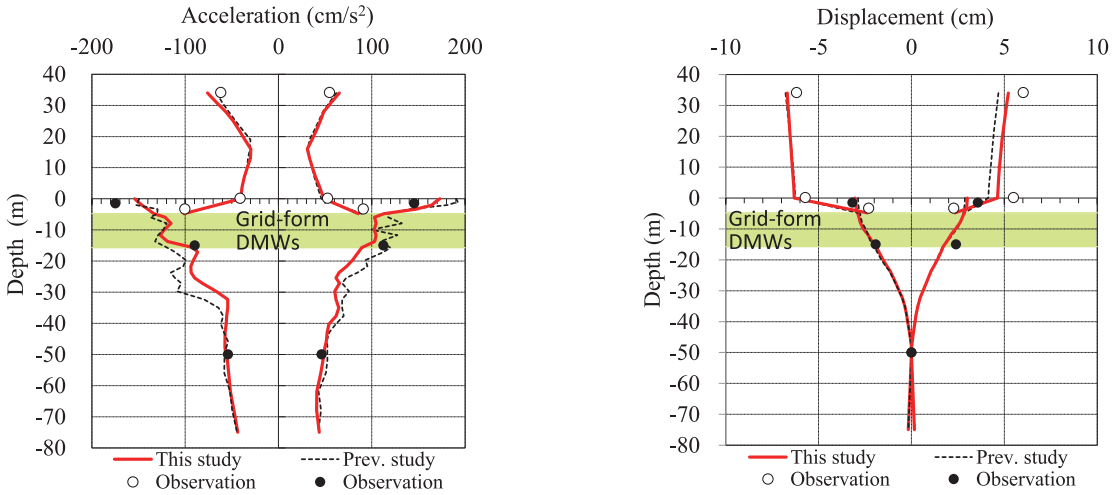

Fig. 12 Profiles of peak response of ground and structure

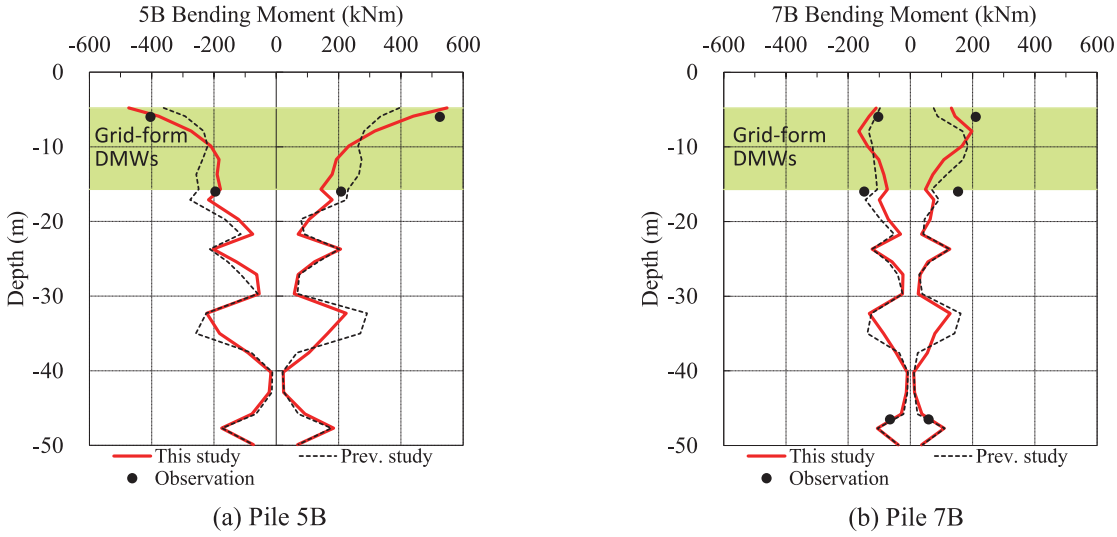

Fig. 13 Profiles of peak bending moment of piles (EW direction)

GL -16m is slightly shifted toward minus direction due to the nonlinearity of the ground. Figure 12 shows the profiles of peak acceleration and relative displacements of the structure and the ground in the EW direction. The displacements are relative to the observation point of the ground at a depth of 50 m shown in Fig. 2. Figure 13 shows the profiles of the peak bending moment of the piles. The results of the observation and the previous study (Shigeno et al., 2015) are also shown in Figs. 12 and 13. It is seen that he results of the peak bending moments near the pile head in the present analysis show better agreement with the observations, and the peak responses of the ground and the structure agree as well with the observations as the previous results. The agreement of the pile bending moment between the analysis and the observations may be important on evaluating the sectional force of the piles under large earthquake load.

4.2 Seismic response analysis under large earthquake load

4.2.1 Input motion

A large earthquake motion was chosen from the so-called Level 2 waves that are notified for a performance-based design in Japanese building design codes. The recurrence interval of the earthquake is considered to be about 500 years. The earthquake motion is defined by acceleration response spectrum, and the NS component of Level 2 motion of Kobe phase data was used as the base input motion, where the Kobe phase data were observed at the Kobe Marine Observatory during the 1995 Hyogoken-Nambu earthquake (referred as the Kobe phase hereafter). The acceleration response spectra of the NS components of Level 2 motion are shown in Fig. 14, and the acceleration waveforms of Level 2 motion in the NS direction are shown in Fig. 15.

4.2.2 Analysis results

Two analysis cases were examined. One is with the grid-form DMWs, and the other is the case without DMWs.

Figure 16 shows the profiles of the peak horizontal acceleration at the center of the superstructure and the raft in the NS direction together with those of the ground at point A. The response of the soil column model is also shown denoted as "far field". The peak ground surface acceleration at the far field was 391 cm/s^2. In the case with DMWs, the peaks were 347 cm/s^2 at the raft and 153 cm/s^2 on the first floor, where the reduction rate by the base isolation system was 44 %. In the case without DMWs, the peaks were 364 cm/s^2 and 123 cm/s^2. The peak acceleration at the raft in the case without DMWs was larger than that in the case with DMWs. This may be attributed to the input loss due to existence of the DMWs.

Figure 17 shows the profiles of the peak horizontal displacement. The displacement in the NS direction is relative to a depth of 49.9 m. The peak displacements at the raft were -11.4 cm and 9.8 cm in the case with DMWs, which are smaller than -15.5 cm and 13.3 cm in the case without DMWs. This indicates that the ground deformation beneath the raft is significantly reduced by the DMWs.

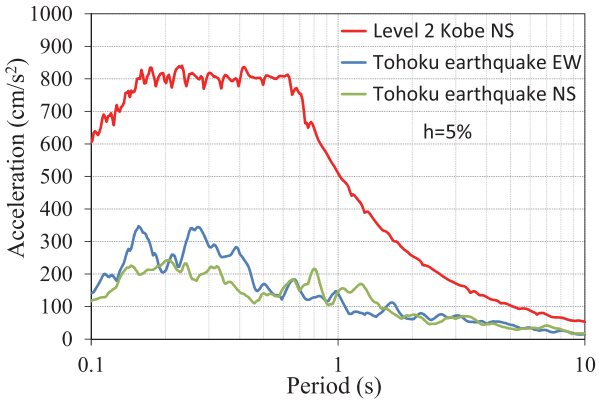

Fig. 14 Acceleration response spectrum, Level 2 wave and the 2011 Tohoku earthquake (at a depth of 75 m)

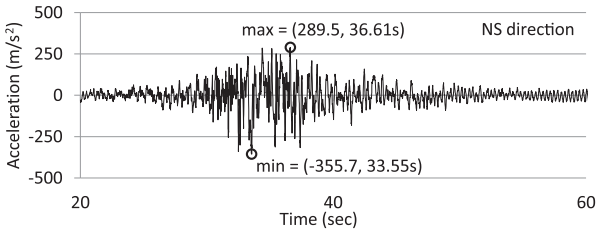

Fig. 15 Input acceleration at a depth of 75 m (2E)

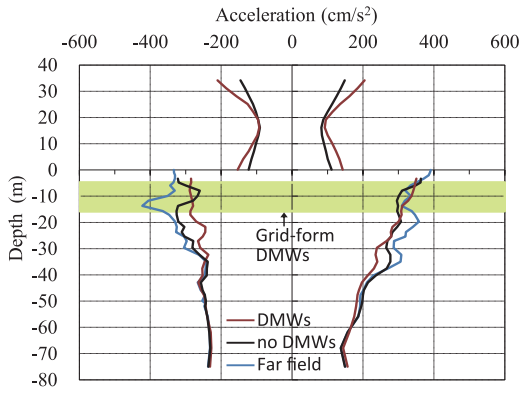

Fig. 16 Peak horizontal acceleration profiles of ground at point A and at far field, and superstructure (NS direction)

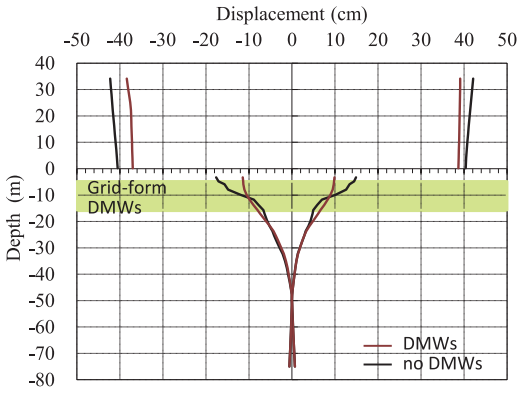

Fig. 17 Peak horizontal displacement profiles of ground at point A and superstructure (NS direction)

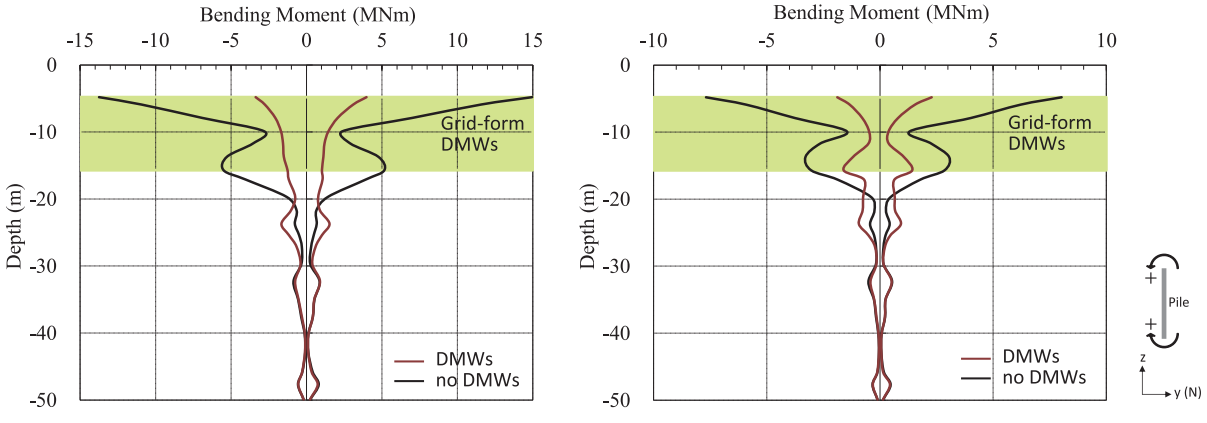

(a) Pile 5B (b) Pile 7B

Fig. 18 Profiles of peak bending moment of piles 5B and 7B (NS direction)

Figure 18 shows the profiles of the peak bending moment in piles 5B and 7B, shown in Fig. 4, in the NS direction. The peak bending moments near the pile head in the case with DMWs are remarkably smaller than those in the case without DMWs. One reason of this result arises because the deformation of the soil enclosed by the DMWs is smaller than that in the case without DMWs.

Figure 19 shows the time histories of the lateral external forces acting on the bottom surface of the raft during the principal motion of 32-39 s. The external forces consist of the inertial forces from the structure (superstructure and raft) as well as the kinematic force induced by ground movements acting on the side of the buried raft. In both the cases, the peak value of the kinematic force from the ground was significantly large in comparison with the inertial forces of the structure. It is also seen that the peak value of the kinematic force in the case with DMWs was larger than that in the case without DMWs.

Figure 20 shows the time histories of the lateral resistance forces of the foundation elements acting on the bottom surface of the raft. The resistance forces are the shear force of the piles at the pile head and that of the soil beneath the raft as well as the shear force of the grid-form DMWs. In the case with DMWs, it is seen that the shear force of the grid-form DMWs was significantly larger than those of the piles and the soil, though the shear force of the piles was quite small. In the case without DMWs, the shear force of the piles was considerably larger than that of the soil.

Figure 21 illustrates the equilibrium of lateral force at the level of the raft bottom in the shaking direction when the total external force in the case with DMWs reached the peak values. In the case with DMWs, the kinematic force from the ground corresponded to about 70% of the total external force. The kinematic force was canceled entirely with the shear force of the DMWs. In the case without DMWs, the kinematic force from the ground corresponded to also about 70% of the total external force, and was carried by both the piles and the soil.

Figure 22 shows the tensile failure zone in the grid-form DMWs, in which the maximum ratio of the maximum principal stress σ_1 to the tensile strength σ_t is larger than 0.95. The value of σ_1 stress is the mean value of eight Gauss points in each element. The tensile failure zone is seen in very limited part around the bottom of the longitudinal walls (parallel to the shaking direction). Meanwhile, the shear failure zone, in which means the maximum ratio of the equivalent stress q to that at failure q_f is larger than 0.95, is not seen in the DMWs.

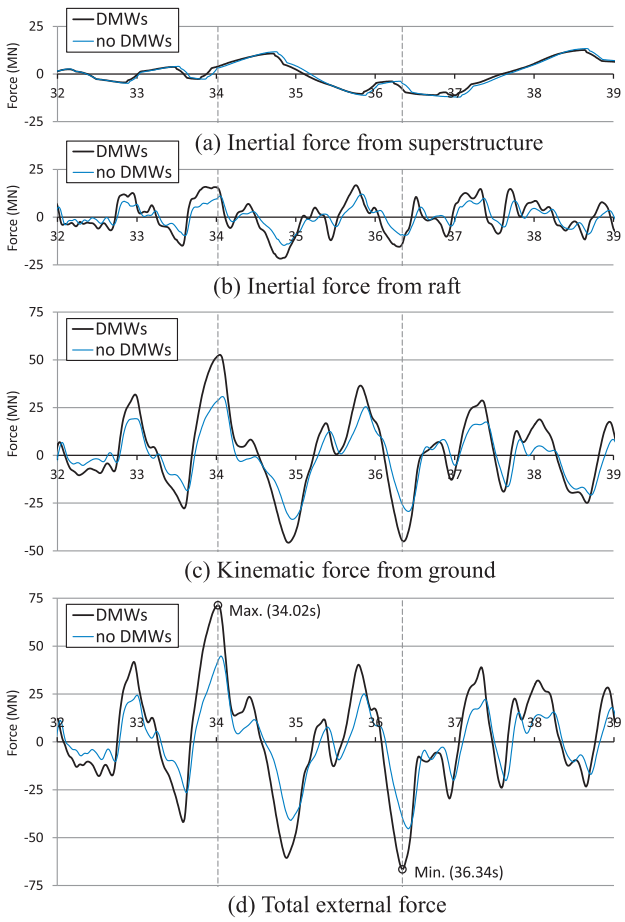

Fig. 19 Time histories of lateral external forces on the bottom surface of raft

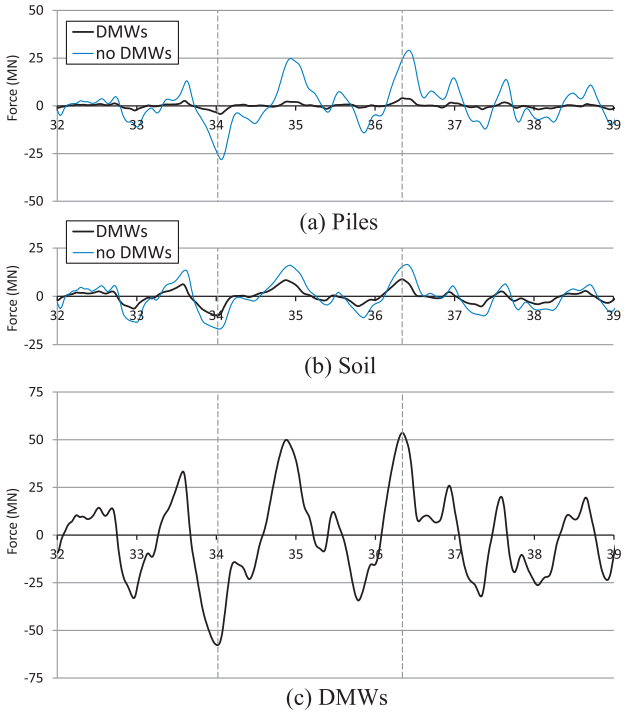

Fig. 20 Time histories of lateral resistance of piles, soil and DMWs on the bottom surface of raft

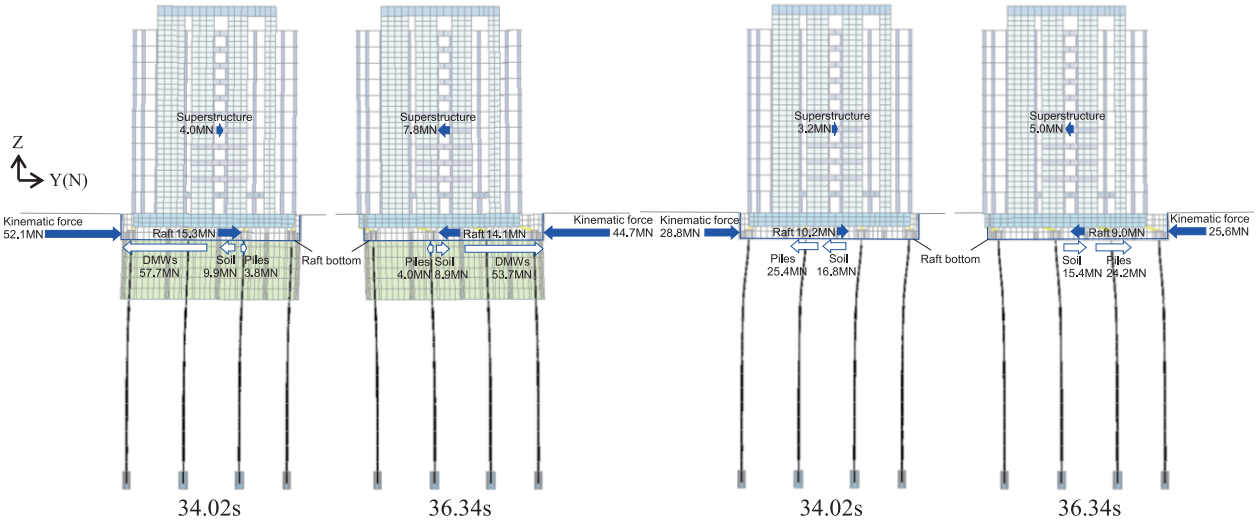

Fig. 21 Equilibrium of lateral force at raft bottom (deformation scale : 10 cm→1 m)

Figure 23 illustrates the deformation mode of the grid-form DMWs with the tensile failure zone at 34.02 and 36.34 s. The dynamic lateral displacements at the mid-length of the transverse walls (perpendicular to the shaking direction) showed significant flexure due to bending near the bottom of the walls, but little flexure near the top of them.

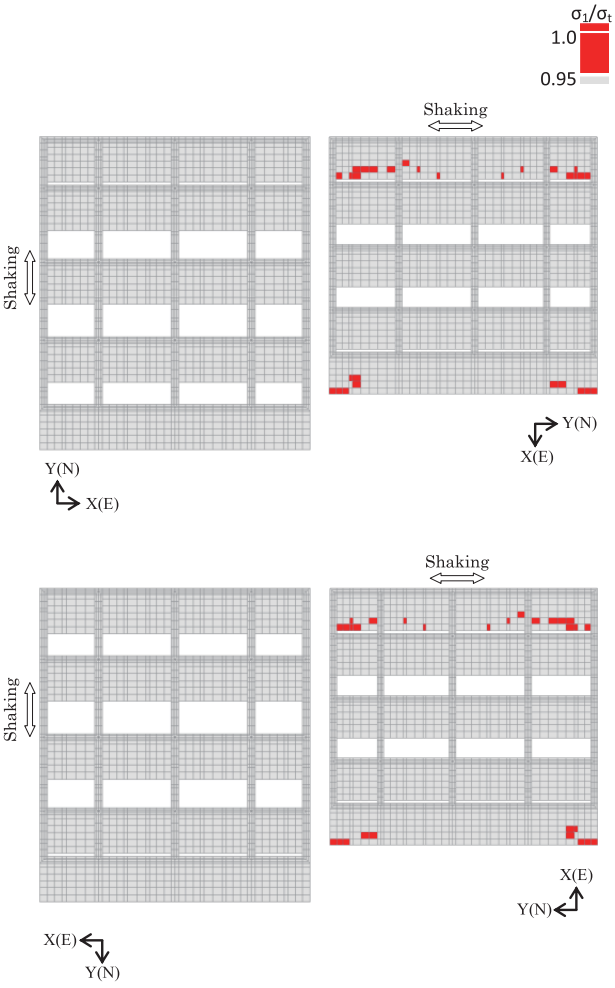

Fig. 22 Tensile failure zones in grid-form DMWs

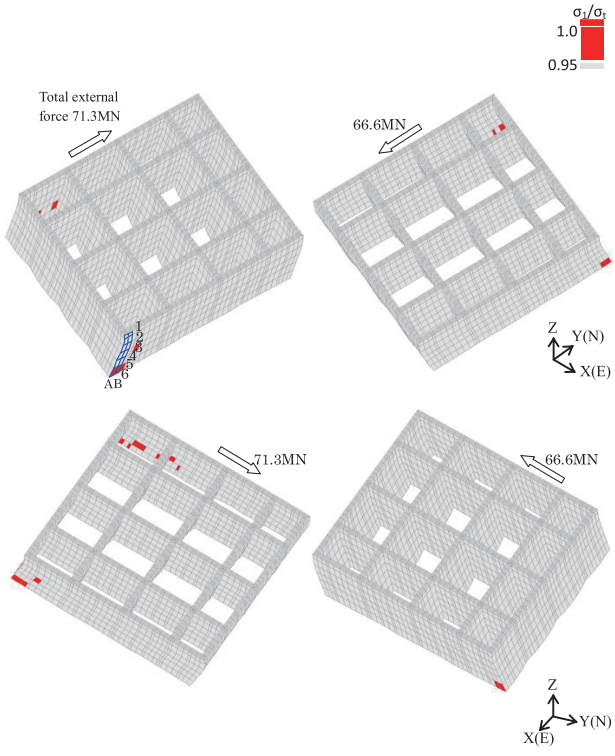

Fig. 23 Deformation modes of grid-form DMWs with tensile failure zones（deformation scale: 1 cm→75 cm）

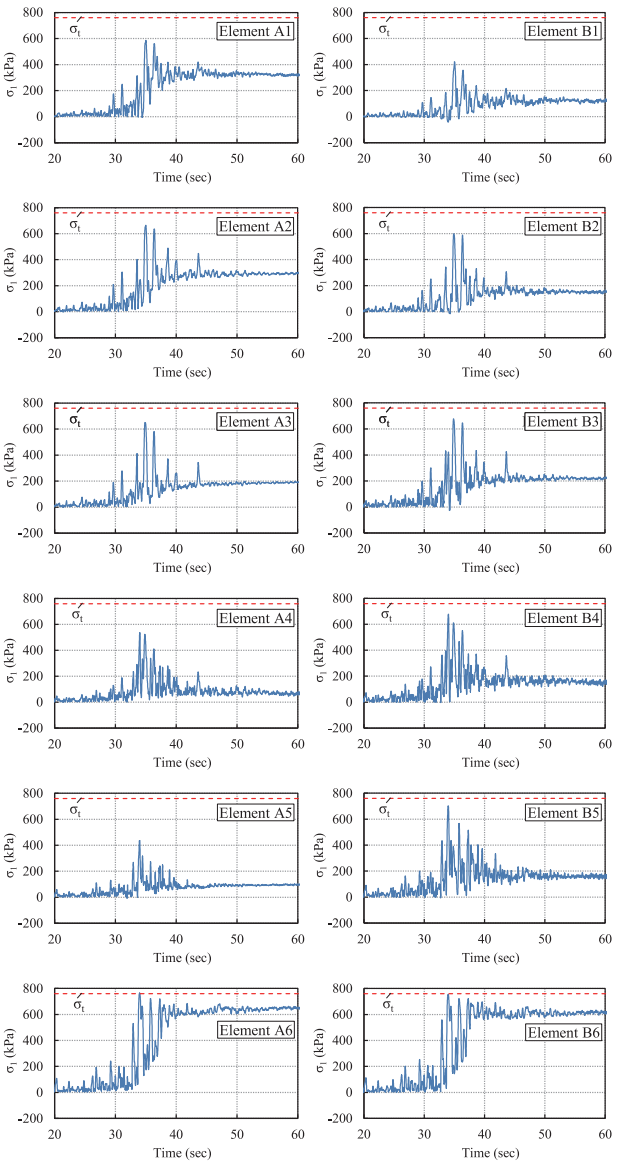

Fig. 24 Time histories of major principal stress in DMW element

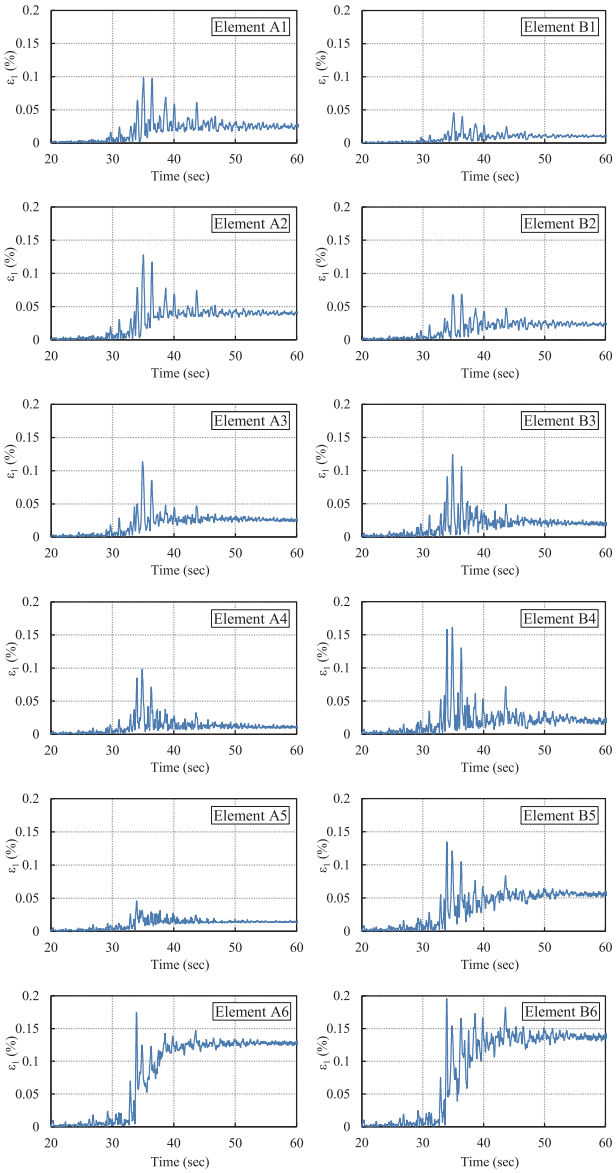

Fig. 25 Time histories of principal tensile strain in DMW element

Figure 24 shows the time histories of the major principal stress σ_1 of the selected elements located near the grid corner of the outer longitudinal wall illustrated in Fig. 23(a) together with the value of the tensile strength. It is seen that the value of σ_1 in elements A6 and B6 (located at the grid corners of the bottom of the longitudinal wall) reached the tensile strength, and the value of remained after the principal motion. The peak values of σ_1 in the other elements were below the tensile strength.

Figure 25 shows the time histories of the principal tensile strain ε_1 of the selected elements. The peak values of ε_1 in elements A6 and B6 were relatively large, up to 0.2%, and remained 0.12-0.15% after the principal motion. The peak values of ε_1 in the other elements were roughly less than 0.15%.

Although the constitutive model used in the present analysis does not consider softening of the stabilized soil after the failure (Namikawa et al., 2007), the analysis results would be acceptable in the engineering point of view because the tensile failure zone is in very limited as shown in Fig. 22.

Figure 26 shows the relationship between the axial force and the bending moment of piles 5B and 7B, together with the design interaction curves of the steel pipe-concrete composite (SC) pile (which is used in the top portion at 12 m). Here, the axial force means the sum of the statically measured pile head load and the maximum and minimum dynamic incremental force in the analysis, and the bending moment means the maximum value along the SC pile in the NS direction. The analysis results show that the maximum bending moments of piles 5B and 7B in the case with DMWs were well below the allowable criterion (the unit stress at the edge of the concrete is in the elastic condition). In contrast, the maximum bending moments in the case

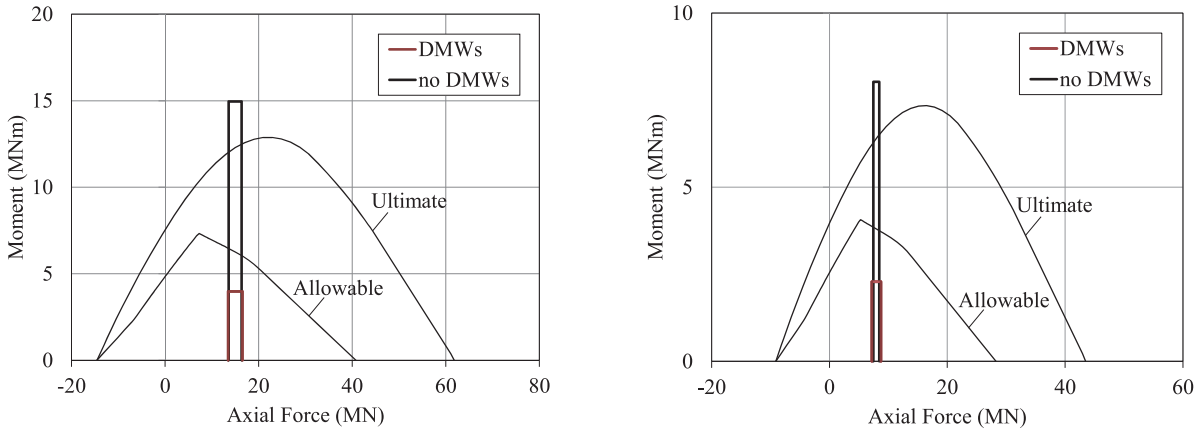

(a) Pile 5B (b) Pile 7B

Fig. 26 NM-relationship of SC piles with calculated values

without DMWs were fairly beyond the ultimate criterion (the unit stress at the edge of the concrete reaches the compressive strength). Hence, the grid-form DMWs were quite effective at reducing pile bending moment to an acceptable level, although the induced stress in the stabilized soil partially reached the tensile strength under the Level 2 earthquake motion. This indicates that the grid-form DMWs can be designed more rationally by the performance-based design method in which a partial failure of the DMWs is accepted, as pointed out by Namikawa et al. (2007). The analysis results also suggested that the 3D FE simulation method employed in this study can provide adequate solutions for the performance-based seismic design of piled rafts with the grid-form DMWs.

5 CONCLUSIONS

Seismic performance of a piled raft foundation with the grid-form DMWs under the large earthquake load was investigated using the 3D nonlinear FE model. First, in order to determine more suitable deformation parameters of the stabilized soil and the unimproved soil to simulate the observation records of the 2011 earthquake (especially the pile bending moment) more accurately, seismic response analysis of the piled raft system was conducted again. Then, the dynamic analysis under the large earthquake was conducted using the more suitable soil deformation parameters. Consequently, it is confirmed that the grid-form DMWs are quite effective at reducing sectional force of the piles to an acceptable level, even if partial tensile failure occurs in the stabilized soil. In addition, the analysis results suggest that the present nonlinear 3D FE method can provide adequate solutions for the performance-based design of the piled raft system under large earthquake loads. These results are consistent with those obtained in the previous study.

REFERENCES

Hamada, J., Shigeno, Y., Onimaru, S., Tanikawa, T., Nakamura, N. and Yamashita, K. (2014): Numerical analysis on seismic response of piled raft foundation with ground improvement based on seismic observation records, Proc. of the 14th IACMAG.

Kuroda, T., Tanaka, H., Tomii, Y. and Suzuki Y. (2001): Evaluation of characteristics of improved soil by deep mixing method of soil stabilization, 2001 Summaries of Technical Papers of Annual Meeting of AIJ (Kanto), 699-700 (in Japanese)

Motojima, M., Hibino S. and Hayashi, M. (1978): Development of computer program for stability analysis of excavation, Central Research Institute of Electric Power Industry Report No 377012 (in Japanese).

Namikawa, T., Koseki, J. and Suzuki, Y. (2007): Finite element analysis of lattice-shaped ground improvement by cement-mixing for liquefaction mitigation, Soils & Foundations, Vol.47, No.3, 559-576.

Onimaru, S., Hamada, J., Nakamura, N. and Yamashita, K. (2012): Dynamic soil-structure interaction of a building supported by piled raft and ground improvement during the 2011 Tohoku Earthquake, Proc. of the 15th World Conference on Earthquake Engineering.

Rokugo, K., Iwasa, M., Suzuki, T. and Koyanagi, W. (1989): Testing methods to determine tensile strain softening curve and

fracture energy of concrete, Fracture Toughness and Fracture Energy, Balkema, 153-163.

Shigeno, Y., Hamada, J. and Nakamura, N. (2014): Hybrid parallelization of earthquake response analysis using K computer, Proc. of the 14th IACMAG.

Shigeno,Y. (2015): Nonlinear analysis of seismic response of a base isolated building on a piled raft foundation with grid-form ground improvement, Proc. of the 15th Asian Regional Conference on Soil Mechanics and Geotechnical Engineering.

Shigeno,Y., Hamada, J., Nakamura, H. and Yamashita, K. (2015): Numerical Analyses of a Piled Raft Foundation with Grid-Form DMWs under Large-Scale Earthquakes, Takenaka Technical Research Report, No.71, 35-47.

Shiomi, T., Yoshizawa, M., Onimaru, S. and Tsukuni, S. (1998): Development of structural analysis system considering non-linear behaviors of soil and structure, Takenaka Technical Research Report, No.54, 1-8 (in Japanese).

Shiomi, T. and Fujiwara, Y. (2014): Liquefaction analysis of Urayasu-site by the multi-hardening model, Proc. of the special symposium of JGS -Overcoming the Great East Japan Earthquake-, 141-145 (in Japanese).

Yamashita, K., Yamada, T. and Hamada, J. (2011): Investigation of settlement and load sharing on piled rafts by monitoring full -scale structures, Soils & Foundations, Vol. 51(3), 513-532.

Yamashita, K., Hamada, J., Onimaru, S. and Higashino, M. (2012): Seismic behavior of piled raft with ground improvement supporting a base-isolated building on soft ground in Tokyo, Soils & Foundations, Vol. 52(5), 1000-1015.

Yamashita, K., Tanikawa, T., Shigeno, Y. and Hamada, J. (2015): Vertical load sharing of piled raft with grid-form deep mixing walls, Proc. of Conference on Deep Mixing 2015, 437-446.

Yamashita, K., Hamada, J. and Tanikawa, T. (2016): Static and seismic performance of a friction piled combined with grid-form deep mixing walls in soft ground, Soils & Foundations, Vol. 56(3), 559-573.